BIOCHEMISTRY
including biophysical chemistry & molecular biology
Article

Biochemistry **2010,** *49,* 3947–3956 3947
DOI: 10.1021/bi1002103

Elucidation of Interactions of Alzheimer Amyloid β Peptides (Aβ40 and Aβ42) with Insulin Degrading Enzyme: A Molecular Dynamics Study†

Ram Prasad Bora and Rajeev Prabhakar*

Department of Chemistry, University of Miami, 1301 Memorial Drive, Coral Gables, Florida 33146

Received February 10, 2010; Revised Manuscript Received April 8, 2010

ABSTRACT: In this study, interactions of the two full-length Alzheimer amyloid β peptides (Aβ40 and Aβ42) with the fully active form of insulin degrading enzyme (IDE) through unrestrained, all-atom MD simulations have been investigated. This enzyme is a Zn-containing metallopeptidase that catalyzes the degradation of the monomeric forms of these peptides, and this process is critical for preventing the progression of Alzheimer's disease (AD). The available X-ray structures of the free and small fragment-bound (Asp1−Glu3 and Lys16−Asp23 of Aβ40 and Asp1−Glu3 and Lys16−Glu22 of Aβ42) mutated forms of IDE and NMR structures of the full-length Aβ40 and Aβ42 have been used to build the starting structures for these simulations. The most representative structures derived from the Aβ40−IDE and Aβ42−IDE simulations accurately reproduced the locations of the active site Zn^{2+} metal and small fragments of the substrates and their interactions with the enzyme from the X-ray structures. The remaining fragments of both the substrates were found to interact with IDE through several hydrogen bonding, π−π, CH−π, and NH−π interactions. In comparison to Aβ40, Aβ42 is more flexible and interacts through a smaller number (17−22) of hydrogen bonds in the catalytic chamber of IDE. Both the substrates adopted more β-sheet character in the IDE environment, an observation that is in line with experiments. Their structural characteristics inside IDE are significantly different than the ones observed in aqueous solution. The atomistic level details provided by these simulations can help in the elucidation of binding and degrading mechanisms of the Aβ peptides by IDE.

Insulin degrading enzyme (IDE)[1] is an ∼110 kDa Zn^{2+}-containing metallopeptidase found in bacteria, plants, and humans (*1*). This enzyme is known to degrade monomeric forms of a wide variety of critical peptides such as insulin, amyloid β (Aβ), amylin, and glucagon (*2*−*5*). All these substrates of IDE are highly diverse in their amino acid sequence and structure but share a common feature; they are amyloidogenic in nature (*3*, *6*−*8*). Among these substrates, the Aβ peptide has been reported to be the major component of plaques that are observed in the brains of patients affected with Alzheimer's disease (AD) (*9*−*11*). The two predominant forms of 40- and 42-amino acid residue Aβ peptides produced in vivo are Aβ40 and Aβ42, respectively, but only the latter has been shown to be a major component (ca. 90%) of the amyloid plaques (*12*−*15*). Accumulating evidence from rodent models and human genetic analysis indicate that IDE activity is critical in determining the level of Aβ (*16*−*19*). The enhanced IDE activity in IDE and amyloid precursor protein (APP) double transgenic mice decreased their Aβ level and prevented the formation of AD pathology (*18*). Therefore, there is a great deal of interest in developing activators of this enzyme for the treatment of AD (*20*−*22*).

The X-ray structures of the free and substrate-bound (Aβ40 and Aβ42) human IDE enzymes have been resolved at 2.8 Å (PDB entry 2JG4), 2.1 Å (PDB entry 2G47), and 2.59 Å (PDB entry 2WK3) resolution, respectively (*7*, *23*, *24*). This enzyme is composed of four homologous domains that are 15−24% similar in sequence. These domains in turn form two functional N- and C-terminal domains (IDE-N and IDE-C, respectively) that are joined by an extended 28-amino acid residue loop to create a large triangular prism-shaped catalytic chamber (35 Å × 34 Å × 30 Å with a height of 36 Å) that can fit peptides smaller than 70 amino acid residues in length (6 kDa) (*7*, *23*−*27*). The internal cavity of IDE-N is largely negative or neutral, whereas IDE-C contains a positive charge (*7*, *23*, *25*). The size and charge distribution of this chamber play important roles in the recognition and binding of substrates. IDE-C facilitates substrate binding, whereas peptide hydrolysis occurs at the active site located in IDE-N (*23*−*25*, *28*). At the active site, the Zn^{2+} metal ion is coordinated to the two histidine residues (His108 and His112) and a glutamate residue (Glu189) (Figure 1a). This site consists of the His-aa-aa-Glu-His (HXXEH) sequence that is the reverse of the classical Zn binding site (HEXXH) observed for the other members of this family such as thermolysin (TLN) (*7*, *23*, *29*−*32*). IDE undergoes a conformational switch from a closed state to an open state to allow the substrates into its catalytic chamber. Inside the chamber, the enzyme contains a conserved substrate binding exosite that is ∼30 Å from the active site (*7*, *25*−*27*). The interactions of the N-terminal residues of substrates with the exosite binding site of the enzyme have been experimentally proposed to facilitate the necessary conformational changes in the substrates inside the chamber for their effective degradation (*7*, *23*, *25*−*27*).

It is noteworthy that in both substrate-bound (Aβ40 and Aβ42) X-ray structures of IDE (PDB entries 2G47 and 2WK3,

†A funding grant (Department of Health Grant 08KN-11) to R.P. from the James and Esther King Biomedical Research Program of the Florida State Health Department is acknowledged.

*To whom correspondence should be addressed. E-mail: rpr@miami.edu. Telephone: (305) 284-9372. Fax: (305) 284-4571.

[1]Abbreviations: IDE, insulin degrading enzyme; Aβ, amyloid β; AD, Alzheimer's disease; MD, molecular dynamics; APP, amyloid precursor protein; PDB, Protein Data Bank.

Published on Web 04/12/2010

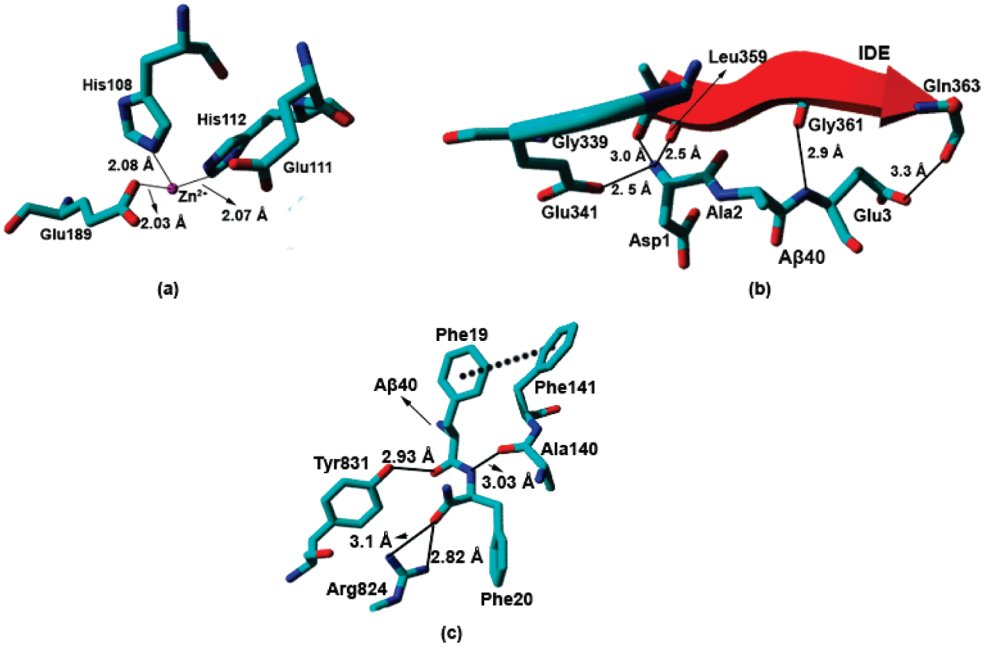

FIGURE 1: (a) X-ray structure of the active site of IDE. (b) Interactions of Aβ40 with the exosite of IDE in the X-ray structure of the IDE−Aβ40 complex. (c) Interactions of the Phe19−Phe20 cleavage site of Aβ40 with IDE in the X-ray structure of the IDE−Aβ40 complex.

respectively), the active site Glu111 is substituted with a Gln residue (*7*, *24*). In addition, the Zn^{2+} ion is missing in the Aβ40-bound structure (PDB entry 2G47) (*7*), and the Aβ42-bound structure (PDB entry 2WK3) belongs to the cysteine free enzyme in which all the cysteine residues have been mutated (*24*). These substitutions rendered the enzyme in the inactive form (*7*, *24*). Furthermore, of the 40 and 42 amino acid residues of Aβ40 and Aβ42, respectively, the X-ray structures consist of only two discrete fragments of the substrates (Asp1−Glu3 and Lys16−Asp23 of Aβ40 and Asp1−Glu3 and Lys16−Glu22 of Aβ42) that form β-sheets with the β6 and β12 strands of IDE, respectively (*7*, *24*). In these structures, the N-terminal Asp1−Glu3 segments of both the peptides interact through hydrogen bonds with the exosite residues (Gly339, Glu341, Leu359, Gly361, and Gln363) of IDE (Figure 1b) (*7*, *24*). The backbone amide group of Asp1 forms hydrogen bonds with the side chain of Glu341 and the backbone carbonyl groups of the Gly339 and Leu359 residues of IDE. In addition, the side chain and the amide backbone of Glu3 were found to make polar interactions with the side chain of Gln363 and backbone carbonyl oxygen atom of Gly361. On the other hand, the larger fragment (Lys16−Asp23 of Aβ40 and Lys16−Glu22 of Aβ42) contains the Phe19−Phe20 hydrolytic cleavage site of the substrates (*7*, *24*, *25*). The Phe19 residue of this site interacts with the aromatic ring of Phe141 through $\pi-\pi$ stacking, and its carbonyl oxygen atom forms a hydrogen bond with Tyr831 of IDE-C. The backbone amide group of Phe20 forms a hydrogen bond with Ala140 (Figure 1c). In addition, Arg824 of IDE-C forms two hydrogen bonds with the backbone of Phe20 (Figure 1c). These interactions may be instrumental in positioning the Phe19−Phe20 cleavage site adjacent to the Zn^{2+} metal center of IDE for hydrolysis (*7*, *24*). It is worth mentioning that the secondary structures and interactions of the remaining fragments (Phe4−Gln15 and Val24−Val40) of Aβ40 and (Phe4−Gln15 and Val24−Ala42) of Aβ42 inside IDE have not been experimentally determined (*7*, *24*).

The elucidation of the binding and degradation mechanisms of the Aβ peptides by IDE requires the atomistic level understanding of the spatial occupancy of the full-length substrates and their interactions inside the catalytic chamber of the enzyme. To accomplish this, in this study the interactions of IDE with two Alzheimer full-length peptides (Aβ40 and Aβ42) through unrestrained, all-atom MD simulations in aqueous solution have been investigated. The free (PDB entry 2JG4) and Aβ40- and Aβ42-bound (PDB entries 2G47 and 2WK3, respectively) X-ray structures of IDE and NMR structures of full-length Aβ40 (PDB entry 1AML) and Aβ42 (PDB entry 1IYT) have been utilized to build the starting models for these simulations. The starting structures for the MD simulations in this study incorporate the active form of the enzyme, including the Zn^{2+} metal center, Glu111, all cysteine residues, and the full-length Aβ40 and Aβ42 substrates. The results gleaned from these simulations will provide a deeper understanding of conformations of full-length Aβ40 and Aβ42 inside the catalytic chamber of IDE and their interactions with the active form of the enzyme.

COMPUTATIONAL PROCEDURE

Structural Modeling. The initial coordinates for the IDE−Aβ40 and IDE−Aβ42 complexes were taken from their X-ray structures (PDB entries 2G47 and 2WK3, respectively), and only the structure of the former is shown in Figure 2a (*7*). In this figure, the active site and both fragments (Asp1−Glu3 and Lys16−Asp23) are projected out. In the starting structure for the IDE−Aβ40 MD simulation, on the basis of its location in the X-ray structure of the IDE−Aβ42 complex (PDB entry 2WK3) (*24*), the missing Zn^{2+} ion is placed in the active site (Figure 2b). The Gln111 residue is also substituted with the catalytically active glutamate residue that functions as a base in the hydrolysis mechanism (*7*, *33*−*35*). This substitution accompanied by the presence of the Zn^{2+} ion converts the enzyme into the catalytically active form. In this form, the Zn^{2+} metal center is directly coordinated to His108, His112, and Glu189 residues, and the fourth vacant site is occupied by a water molecule (not shown in the figure) that is activated for the hydrolysis of a peptide bond. Since all the cysteine residues are mutated in the Aβ42-bound X-ray structure of IDE (PDB entry 2WK3) (*24*), only the active site−substrate interactions were taken from this structure

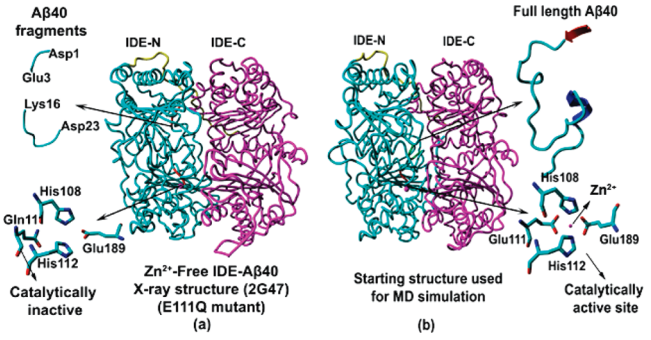

FIGURE 2: (a) X-ray structure of the IDE−Aβ40 complex. (b) Starting structure of the IDE−Aβ40 complex used in MD simulations.

and the coordinates of IDE extracted from the Aβ40-bound structure (PDB entry 2G47) (*7*). The initial coordinates of the full-length Aβ40 and Aβ42 peptides were obtained from the NMR structures [PDB entries 1AML for Aβ40 (*36*) and 1IYT for Aβ42 (*37*)]. This structure (PDB entry 1AML) of Aβ40 was also used in characterizing the X-ray structure of the IDE−Aβ40 complex (*7*), while the NMR structure of Aβ42 (PDB entry 1IYT) obtained in the 80:20 (v/v) HFIP/H_2O mixture has been utilized as a starting point in several MD simulations (*38*−*40*). Recently, another NMR structure of this peptide (PDB entry 1Z0Q) has been determined in a 30:70 (v/v) HFIP/H_2O solution (*41*). An analysis of these two NMR structures of Aβ42 indicates that, except at the C-terminus, both of them are quite similar (Figure 1 in the Supporting Information).

The models for the IDE−Aβ40 and IDE−Aβ42 complexes for the MD simulations were generated in a multistep process. In the first step, the NMR structures of both full-length Aβ40 and Aβ42 substrates were docked inside the catalytic chamber of IDE. In the docking process, the spatial occupancy and interactions of Asp1−Glu3 and Lys16−Asp23 of Aβ40 and Asp1−Glu3 and Lys16−Glu22 of Aβ42 fragments of the substrates with the enzyme were retained from the corresponding X-ray structures (PDB entries 2G47 and 2WK3 for Aβ40 and Aβ42, respectively). In the second step, only the remaining segments of the substrates were energy minimized by keeping the entire enzyme and both fragments of the substrates from the X-ray structures of the IDE−Aβ40 and IDE−Aβ42 complexes fixed. The minimized structures were then used as the starting structures for MD simulations that were performed in two phases. In this first 5 ns long equilibration phase, the entire system was equilibrated by constraining only the catalytic center of the IDE enzyme and both segments of the substrate from the X-ray structures. These constraints retained the interactions of the substrate with the active site and exosite during equilibration. The structures obtained at the end of the 5 ns equilibration phase were subsequently used as the initial structure for the next 20 ns long phase known as the production phase. In the production phase of simulations, no geometrical constraints were imposed. To observe the influence of the aqueous medium that is substantially different from the IDE environment on the secondary structural features of Aβ40 and Aβ42, separate 20 ns MD simulations were also performed on the NMR structures of these peptides (PDB entries 1AML and 1IYT, respectively) in aqueous solution.

Computational Details. All MD simulations were performed using GROMACS (*42*, *43*) with GROMOS force field 53A5 (*44*). The initial structures of the IDE−Aβ40 and IDE−Aβ42 complexes were placed in the center of a periodic box with dimensions of 8.6 nm × 8.2 nm × 8.2 nm that extended 14 Å from these complexes on each side. These boundaries eliminate unwanted effects from the applied periodic boundary conditions (PBC). In addition, sodium and chloride ions were randomly placed to neutralize the system under study. The enzyme−substrate models contain ca. 16500 atoms that are solvated by approximately 30000 simple point charge (SPC) water molecules (*45*), i.e., 106500 atoms in total. Nonpolar hydrogen atoms in these models are treated implicitly using the united atom approach, where they are collapsed into the connected heavy atom.

The initial structures were further energy minimized with the steepest descent method for 3000 steps by releasing all the constraints. All the 20 ns production phase MD simulations were conducted with a constant number of particles (N), pressure (P), and temperature (T), i.e., NPT ensemble. The SETTLE algorithm was used to constrain the bond length and angle of the water molecules (*46*), while the LINCS algorithm was utilized to constrain the bond length of the enzyme (*47*). Particle mesh Ewald (PME) was employed to include the contributions of long-range interactions (*48*, *49*). A constant pressure of 1 bar was applied with a coupling constant of 1.0 ps; the peptide, water molecules, ions, and the zinc metal ion are coupled separately to a bath at 300 K with a coupling constant of 0.1 ps.

The trajectories are computed for each model with a time step of 2 fs, and the data are saved every 500 steps for analysis. The ionizable residues are set to their normal ionization states at pH 7. The tools available in GROMACS are utilized to analyze the MD trajectories. The contact maps and the most representative structures obtained from the cluster analysis have been used for the structural elucidation. In the contact maps, a contact for a pair of amino acid side chains is considered to be formed when a minimal distance between any pair of their atoms is less than 0.5 nm. The most representative structures are derived from the cluster analysis, where the trajectories are analyzed by grouping structurally similar frames [root-mean-square deviation (rmsd) cutoff of 0.30 nm] (*50*), and the frame with the largest number of neighbors is denoted as a middle structure that represents that particular cluster. YASARA (*51*) was used for visualization and for the preparation of the structural diagrams presented in this study.

RESULTS AND DISCUSSION

In this study, 20 ns unrestrained MD simulations on the Aβ40 and Aβ42 substrates and their complexes with IDE (IDE−Aβ40 and IDE−Aβ42) have been performed in an aqueous solution. The primary objective of this study is to elucidate the structures and interactions of the full-length Aβ40 and Aβ42 substrates inside the catalytic chamber of IDE at the atomic level. The binding of Aβ40 and Aβ42 to the chamber was not found to alter the overall structure of the enzyme in the simulations. The rmsd values of the backbone α-carbon atoms from the simulations clearly indicate that both enzyme−substrate complexes (Figure 3a) and the individual substrates inside IDE (Figure 3b) attained stable conformations only after 6 ns simulations. In the thermodynamically equilibrated region, no trajectories exhibit significant changes and the overall rmsd's remain below 0.30 nm.

IDE−*Aβ40 Interactions*. A superposition of the conformation of full-length Aβ40 derived from the most representative structure of the IDE−Aβ40 simulation with the Asp1−Glu3 and Lys16−Asp23 fragment-containing X-ray structure (PDB entry 2G47) is shown in Figure 4a. This structure explicitly shows that

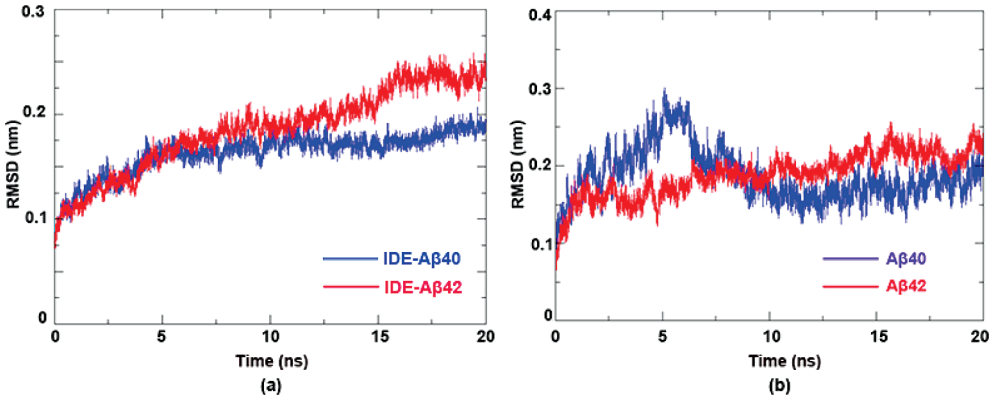

FIGURE 3: (a) rmsd's of the IDE−Aβ40 and IDE−Aβ42 trajectories plotted vs time. (b) rmsd's of Aβ40 and Aβ42 derived from the IDE−Aβ40 and IDE−Aβ42 trajectories, respectively.

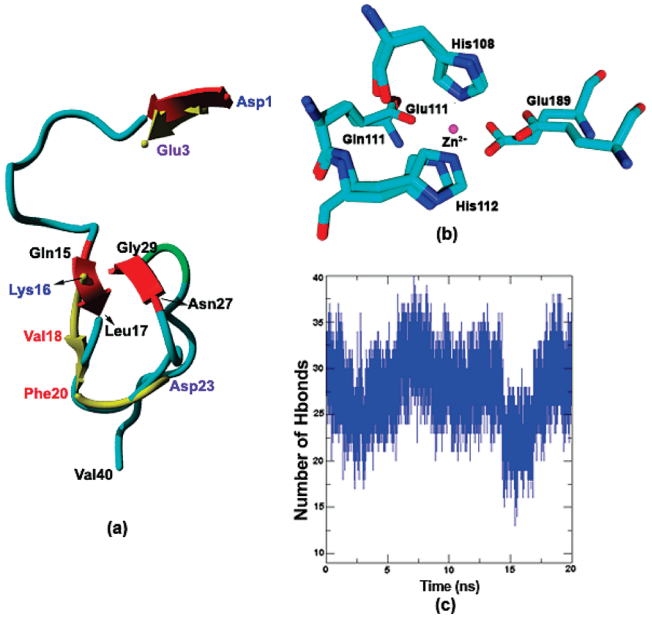

FIGURE 4: (a) Superposition of the conformation of Aβ40 derived from the most representative structure of the IDE−Aβ40 simulation with the corresponding X-ray structure (yellow). (b) Superposition of the conformation of the Zn^{2+} metal center derived from the most representative structure of the IDE−Aβ40 simulation with the corresponding X-ray structure. (c) Time-dependent variation of the number of hydrogen bonds between Aβ40 and IDE.

the locations of both fragments are accurately reproduced in the MD simulations. A superposition between the X-ray and simulated structures of the Zn^{2+} metal center also validates the simulation (Figure 4b). In this structure, similar to the X-ray structure, the residues in the first coordination shell (His108, His112, and Glu189) lie within bond forming distance of the Zn^{2+} ion.

Throughout the simulation, Aβ40 was found to interact with the amino acid residues of the catalytic chamber of IDE via a large number (25−30) of hydrogen bonds (Figure 4c). The MD simulations indicate that the NMR structure of the Aβ40 substrate undergoes significant secondary structural changes and loses its initial helical character inside IDE. The snapshots of the conformational transformations at 5, 10, 15, and 20 ns are shown in Figure 5a. In the first 5 ns of the simulation, the Asp1−Glu3 and Ser8−Glu11 segments of Aβ40 adopt β-sheet conformation, while the Ala30−Leu34 region attains an α-helix character. We observed that interactions of the N-terminal residues of the substrate with the enzyme remain conserved and the Asp1−Glu3 region retains its initial β-sheet character during the simulation (Figure 5a). However, the β-sheet and α-helix structures of the Ser8−Glu11 and Ala30−Leu34 fragments, respectively, are stable only for the first 6 ns; after that, they transform into a random coil and loop structure, respectively. The Gln15−Leu17 and Asn27−Gly29 segments were found to interact through hydrogen bonds with each other and form stable antiparallel intramolecular β-sheet structures after 12 ns of the simulation (Figure 5a). This conformation may be stabilized by the interactions of the Glu11−Val12 and Phe19−Glu22 regions, which encompass the Gln15−Leu17 fragment of the substrate with IDE (Table 1). The His13−Gly25 and Ile31−Val36 regions also transform from the initial α-helical conformation (Figure 2 of the Supporting Information) to the random coil and β-sheet structures, respectively, in the IDE environment.

The contact map of Aβ40 from the most representative structure of the Aβ40−IDE simulation shows that it forms a large number of intramolecular interactions particularly in the Glu15−Phe19 and Ala21−Lys28 regions (Figure 5b). In the X-ray structure of the IDE−Aβ40 complex, the N-terminal residues (Asp1−Glu3) of Aβ40 are observed to form hydrogen bonds with the exosite residues (Glu341, Gly339, Leu359, Gly361, and Gln363) and the Phe19−Phe20 cleavage site interacts with Ala140, Phe141, Arg824, and Tyr831 of IDE (Figure 1b,c) (*7*). These interactions have been experimentally proposed to be responsible for the orientation and folding of the substrate inside IDE (*7*, *8*, *24*, *25*, *27*). All of them have also been observed in the most representative structure derived from the IDE−Aβ40 simulation using the full-length peptide (Figure 5c,d and Table 1). During the simulation, the side chains of Asp1 and Glu3 of Aβ40 reorient in such a way that the carbonyl oxygen and the side chain nitrogen atoms of Ala2 form a hydrogen bond with the side chain nitrogen atom of Gly361 and the hydroxyl (OH) group of Tyr609, respectively (Figure 5c). The movement of the side chain of Glu3 also allows the carbonyl oxygen atom to establish polar interactions with Gln363. These interactions at the exosite stabilize the β-sheet structure in the Asp1−Glu3 region of Aβ40. The carbonyl (C═O) and amine (NH_2) groups of the backbones of Gln15 and Leu17 were observed to form hydrogen bonds with the backbone amine and carbonyl groups of Gly29 and Asn27, respectively. These interactions might be responsible for the transformation of the Gln15−Leu17 and Asn27−Gly29 fragments from random coil to β-sheet conformation (Figure 5a). In addition, the carbonyl oxygen (C═O) of Phe19 was found to coordinate to the Zn^{2+} ion (Zn^{2+}−O distance of 2.03 Å).

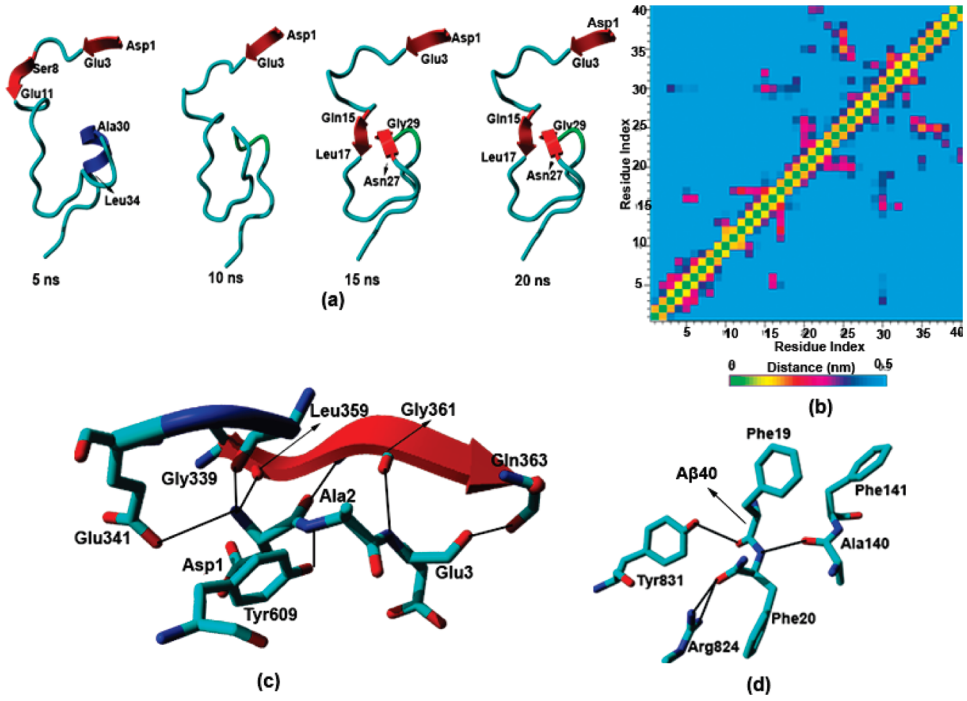

FIGURE 5: (a) Snapshots of the secondary structure of Aβ40 inside the IDE chamber at 5, 10, 15, and 20 ns. (b) Contact map of Aβ40 inside the IDE chamber. (c) Interactions of Aβ40 with the exosite of IDE in the most representative structure obtained from the IDE−Aβ40 simulation. (d) Interactions of the Phe19−Phe20 cleavage site of Aβ40 with IDE in the most representative structure obtained from the IDE−Aβ40 simulation.

This interaction has been reported to activate the scissile Phe19−Phe20 peptide bond for hydrolysis (*34*).

In addition to the aforementioned specific interactions, the MD simulations revealed several intermolecular hydrogen bonding and hydrophobic interactions between the remaining Aβ40 peptide and IDE (Tables 1 and 2). The backbone carbonyl and amine groups of the substrate are mainly involved in forming hydrogen bonds with IDE. The Asp1−Val12, Phe19−Glu22, and Ile32−Val40 regions of Aβ40 participate in the formation of hydrogen bonds with IDE (Table 1). In particular, the C-terminal Val36, Gly38, Val39, and Val40 residues of Aβ40 interact with the Ser137, Ser137, Ser128, and Thr825 residues of IDE, respectively. The Phe4 and Tyr10 residues of the substrate form $\pi-\pi$ interactions with Tyr454 and Phe215 of IDE, respectively (Table 2). Tyr10 also coordinates through a CH$-\pi$ interaction with Phe370. These interactions may play key roles in the observed transformations in the initial secondary structure of Aβ40 inside the IDE chamber.

The overall secondary structure of Aβ40 inside IDE was found to be quite different from that in the aqueous environment. In aqueous solution, the Glu11−Lys16 and Glu22−Asn27 fragments of this peptide adopt α-helical conformations, while the rest of the peptide forms random coil and loop structures during the 20 ns simulation (Figure 3 of the Supporting Information). However, in marked contrast to its behavior in the aqueous medium, Aβ40 completely loses its α-helical character after simulation inside IDE for only 6 ns and forms β-sheet structures in the Asp1−Glu3, Gln15−Leu17, and Asn27−Gly29 regions. These structural transformations might be critical for its degradation by IDE.

IDE−Aβ42 Interactions. Because of the presence of the two additional hydrophobic residues (Ile41 and Ala42) in Aβ42, the mode of interaction and the structural transformations for this peptide inside IDE are markedly different from those observed for the Aβ40 substrate. A superposition of the conformation of full-length Aβ42 derived from the most representative structure of the IDE−Aβ42 simulation with the X-ray structure (PDB entry 2WK3) is shown in Figure 6a. In this structure, the position of the Asp1−Glu3 fragment deviates from that in the X-ray structure, while that of the longer Lys16−Glu22 fragment is well conserved. Similar to the IDE−Aβ40 case, here the Zn^{2+} metal center was found to retain its position from the X-ray structure (Figure 6b). In comparison to Aβ40, Aβ42 is more flexible inside IDE and forms a smaller number (17−22) of intermolecular hydrogen bons with IDE (Figure 6c). However, in the C-terminal region, this substrate forms more hydrogen bonds with IDE than Aβ40. The contact map of the most representative structure indicates that Aβ42 also generates fewer intramolecular interactions inside IDE than Aβ40 (Figure 6d).

During the simulations, like Aβ40, the mostly helical NMR structure of Aβ42, in Asp7−His14, Phe19−Ser26, and Lys28−Gly38 regions (Figure 2 of the Supporting Information), goes through substantial structural changes. The snapshots of the transformation of Aβ42 inside the chamber for 5, 10, 15, and 20 ns are shown in Figure 7a. The Tyr10−Gln15 fragment of this peptide largely retains its α-helical character throughout the simulation, whereas Aβ40 completely lost its α-helical character. The overall percentage of the β-sheet character in Aβ42 is lower than that in Aβ40, but in the former, the Phe20−Ala21 region exists in the β-sheet conformation. In Aβ42, the Gln15−Leu17 and Asn27−Gly29 regions adopt a random coil structure, while they form an antiparallel β-sheet in Aβ40.

The hydrogen bonding interactions in the IDE−Aβ42 complex are also different from those in the IDE−Aβ40 case, particularly at the N- and C-termini of the substrate. Because of the large structural rearrangement and higher flexibility of Aβ42 inside IDE, the hydrogen bonding network between the N-terminal residues of this peptide and the exosite residues is

Table 1: List of Hydrogen Bonding Interactions between IDE and Substrates (Aβ40 and Aβ42)

Aβ40 (residue)	atom	IDE (residue)	atom	Aβ42 (residue)	atom	IDE (residue)	atom
Asp1	N	Gly339	O	Asp1	OD2	Glu341	N
	N	Glu341	OE1		N	Leu359	O
	N	Leu359	O		OD1	Tyr609	OH
	O	Gly361	N				
Ala2	N	Tyr609	OH	Ala2	−	−	−
Glu3	O	Gln363	N	Glu3	−	−	−
	N	Gly361	O				
Phe4	−	−	−	Phe4	−	−	−
Arg5	NH2	Glu365	OE1	Arg5	NH1	Asn605	OD1
					N	Tyr609	OH
					NH2	Glu612	OE1
					NH2	Tyr618	OH
His6	O	Gln363	NE2	His6	−	−	−
	NE2	Leu455	N				
Asp7	OD2	Tyr444	OH	Asp7	−	−	−
Ser8	O	Gly366	N	Ser8	OG	Lys436	NZ
Gly9	−	−	−	Gly9	−	−	−
Tyr10	−	−	−	Tyr10	−	−	−
Glu11	OE1	Ser96	OG	Glu11	OE1	Lys364	NZ
	O	Glu145	N		OE2	Lys364	NZ
	OE2	Lys206	NZ				
Val12	O	Ser143	OG	Val12	−	−	−
His13	−	−	−	His13	−	−	−
His14	−	−	−	His14	−	−	−
Gln15	−	−	−	Gln15	OE1	Trp199	NE1
Lys16	NZ	Asn196	OD1	Lys16	−	−	−
	O	Asn193	ND2				
Leu17	−	−	−	Leu17	O	Asn193	ND2
Val18	−	−	−	Val18	−	−	−
Phe19	O	Tyr831	OH	Phe19	O	Tyr831	OH
Phe20	N	Ala140	O	Phe20	N	Ala140	O
	O	Arg824	NH1, NH2		O	Ala140	N
Ala21	O	Asn139	ND2	Ala21	N	Asn139	OD1
	N	Asn139	OD1		−	−	−
Glu22	OE1	Tyr831	OH	Glu22	−	−	−
	OE1	Lys192	NZ				
Asp23	−	−	−	Asp23	OD1	Ser835	N, OG
Val24	−	−	−	Val24	−	−	−
Gly25	O	Lys192	NZ	Gly25	−	−	−
Ser26	−	−	−	Ser26	−	−	−
Asn27	−	−	−	Asn27	−	−	−
Lys28	−	−	−	Lys28	−	−	−
Gly29	−	−	−	Gly29	−	−	−
Ala30	−	−	−	Ala30	−	−	−
Ile31	−	−	−	Ile31	−	−	−
Ile32	O	Arg429	NE, NH2	Ile32	−	−	−
Gly33	−	−	−	Gly33	−	−	−
Leu34	O	Arg431	NH1	Leu34	O	Asn139	ND2
Met35	−	−	−	Met35	SD	Arg824	NH2
					O	Asn139	ND2
Val36	O	Ser137	OG	Val36	−	−	−
Gly37	−	−	−	Gly37	O	Ser138	N
Gly38	N	Ser137	OG	Gly38	O	Gln813	NE2
Val39	O	Ser128	OG	Val39	−	−	−
Val40	OT2	Thr825	OG1	Val40	N	Gln813	OE1
	OT1	Ser128	OG				
	OT1	Asn821	ND2				
				Ile41	O	Arg839	NH1
				Ala42	−	−	−

disrupted. This disruption facilitates the formation of the random coil structure in the Asp1−Glu3 fragment of Aβ42. In contrast, this region exists in the β-sheet conformation in Aβ40. The side chain oxygen atom of Asp1 (OD1) forms a hydrogen bond with Tyr609 of IDE (Figure 7b). At the exosite, the backbone amide group of the former interacts with the carbonyl oxygen atom of Leu359, while the side chain oxygen (OD2) forms a hydrogen bond with the backbone amide of Glu341. However, the Phe4 residue of Aβ42 coordinates through $\pi-\pi$ interactions with His336, while it interacts with the Tyr454 residue in Aβ40. In addition, this residue makes CH$-\pi$ interactions with both His332 and Tyr609. Unlike Tyr10 of Aβ40, here this residue

Table 2: List of $\pi-\pi$, CH$-\pi$, and NH$-\pi$ Interactions between IDE and Substrates (Aβ40 and Aβ42)

Aβ40 (residue)	IDE (residue)	interaction	Aβ42 (residue)	IDE (residue)	interaction
Phe4	Tyr454	$\pi-\pi$	Phe4	His336	$\pi-\pi$
Tyr10	Phe215	$\pi-\pi$		Tyr609	$\pi-\pi$
	Phe370	CH$-\pi$		His332	CH$-\pi$
Phe19	Phe141	CH$-\pi$	His13	Arg431	NH$-\pi$
Phe20	Phe115	$\pi-\pi$	Lys16	Phe202	NH$-\pi$
			Phe19	Phe141	CH$-\pi$

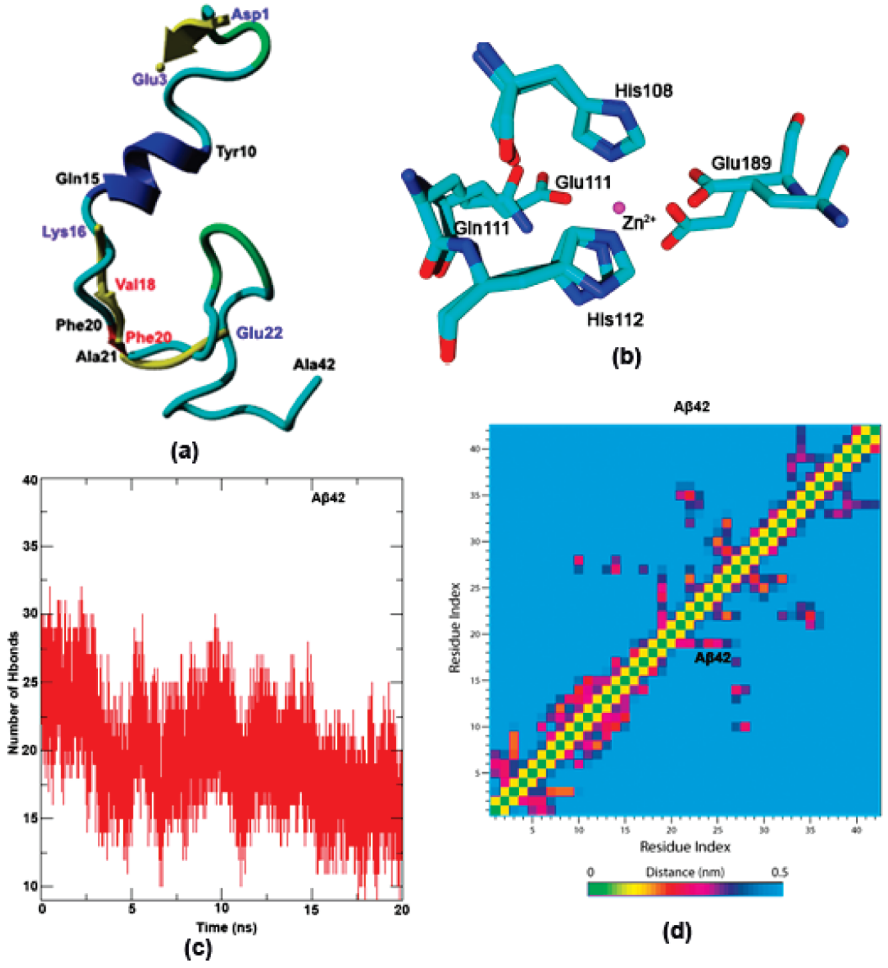

FIGURE 6: (a) Superposition of the conformation of Aβ42 derived from the most representative structure of the IDE$-$Aβ42 simulation with the corresponding X-ray structure (yellow). (b) Superposition of the conformation of the Zn^{2+} metal center derived from the most representative structure of the IDE$-$Aβ42 complex with the corresponding X-ray structure. (c) Time-dependent variation of the number of hydrogen bonds between Aβ42 and IDE. (d) Contact map of Aβ42 inside the IDE chamber.

does not interact with IDE. His13 and Lys16 of Aβ42 associate with Arg431 and Phe202 of IDE, respectively, through NH$-\pi$ hydrogen bonds. Similar to the Aβ40 substrate, Phe19 of the Phe19$-$Phe20 cleavage site of Aβ40 interacts through the CH$-\pi$ interaction with Phe141. However, the interaction of the carbonyl oxygen of Phe20 with Arg824 of IDE is disrupted because of the reorientation of its backbone atoms and leads to the formation of an additional hydrogen bond with Ala140 (Figure 7c). This slight reorganization in the bonding environment does not alter the spatial occupancy of the scissile Phe19$-$Phe20 peptide bond, and it is still accessible to the Zn^{2+} metal center for hydrolysis. The atomistic level details provided by the simulations elucidate the roles of the active site residues in the positioning and stabilizing of the Phe19$-$Phe20 cleavage site of the Aβ40 and Aβ42 substrates. For instance, Ala40, Tyr831, and Arg824 are involved in placing the scissile peptide bond adjacent to the Zn^{2+} metal center, and Glu182 and Thr220 stabilize the metal center by forming hydrogen bonds with the His112 and His108 ligands of the Zn^{2+} ion. This information can also be utilized in building models for mechanistic studies using the quantum mechanics/molecular mechanics (QM/MM) approach. In addition to the hydrogen bonds observed in the X-ray structure, the rest of the peptide associates through several hydrogen bonds with IDE (Table 1). For instance, the C-terminal residues Gly37, Gly38, Val40, and Ile41 of Aβ42 form hydrogen bonds with Ser138, Gln813, and Arg839 of IDE.

These results explicitly show that, in contrast to the IDE$-$Aβ40 complex, the hydrogen bonding network at the exosite of IDE is not well conserved in the IDE$-$Aβ42 complex.

Similar to the Aβ40 peptide, the overall secondary structure of Aβ42 inside IDE was also found to be different than in the aqueous environment. In aqueous solution, the α-helical character

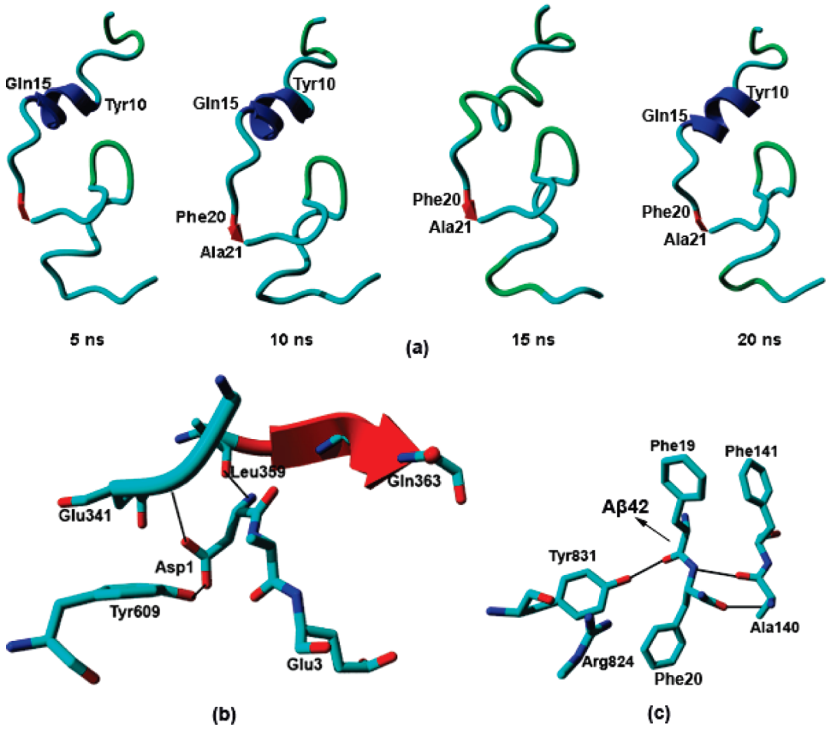

FIGURE 7: (a) Snapshots of the secondary structure of Aβ42 inside the IDE chamber at 5, 10, 15, and 20 ns. (b) Interactions of Aβ42 with the exosite of IDE in the most representative structure obtained from the IDE−Aβ42 simulation. (c) Interactions of the Phe19−Phe20 cleavage site of Aβ42 with IDE in the most representative structure obtained from the IDE−Aβ42 simulation.

of the peptide is significantly reduced and the Leu34−Val36 and Val39−Ile41 regions are transformed into the β-sheet form. In this medium, only the Gln15−Val18 and Ala21−Gly25 fragments exist in α-helical form and the remaining fragments adopt a random coil conformation. On the other hand, inside IDE, the Tyr10−Gln15 and Phe20−Ala21 regions form α-helix and β-sheet structures, respectively, and the remaining peptide exists in random coil and loop structures.

In the presence of the Ile41−Ala42 dipeptide, the hydrophobicity of Aβ42 is increased and, because of the differences in the intra- and intermolecular interactions, it folds in a manner quite different from that of Aβ40 in diverse environments. The starting NMR structures of Aβ40 and Aβ42 used in the simulations (Figure 1 of the Supporting Information) and their equilibrated structures in aqueous solution (Figure 2 of the Supporting Information) adopt substantially different conformations. Furthermore, the most representative structures derived from the MD simulations show that their structures inside IDE are also very different from each other (Figures 4a and 6a). Because of the differences in its structure and intramolecular interactions, Aβ42 interacts with IDE in a manner significantly different from that of Aβ40.

SUMMARY AND CONCLUSIONS

In this study, the interactions of the two full-length Alzheimer amyloid β peptides (Aβ40 and Aβ42) with IDE through unrestrained, all-atom MD simulations in aqueous solution have been investigated. The available X-ray structures of the free (PDB entry 2JG4) and small fragments of Aβ40- and Aβ42-bound (PDB entries 2G47 and 2WK3, respectively) mutated forms of IDE and NMR structures of full-length Aβ40 (PDB entry 1AML) and Aβ42 (PDB entry 1IYT) have been used to develop the starting structures for the simulations. The most representative structures derived from the Aβ40−IDE and Aβ42−IDE simulations accurately reproduced the spatial occupancies of the active site Zn^{2+} metal and small fragments of the substrates (Asp1−Glu3 and Lys16−Asp23 of Aβ40 and Asp1−Glu3 and Lys16−Glu22 of Aβ42). Moreover, all the interactions of these fragments with IDE observed in the X-ray structure were retained in the MD simulations. The remaining regions of both the substrates that were missing in the X-ray structures were found to form several hydrogen bonding, $\pi-\pi$, CH$-\pi$, and NH$-\pi$ interactions with IDE. In comparison to the 25−30 hydrogen bonds formed by Aβ40, Aβ42 was observed to be more flexible and interact through a smaller number (17−22) of hydrogen bonds with IDE. From their starting structures, both Aβ40 and Aβ42 were found to adopt more β-sheet character in the IDE environment. This observation is in line with the experimental suggestion that inside IDE these substrates adopt β-sheet conformations that facilitate their degradation by the enzyme. These structural characteristics are significantly different from the ones these peptides adopt in an aqueous solution. Although the canonical ensemble sampling performed in this study correctly reproduced the structural features from the X-ray structures, the prediction of the free energy can be further improved by the application of the recently developed orthogonal space random walk method (*52*). This method synchronizes the order parameter move and conformational relaxation by overcoming the "Hamiltonian" lagging observed with conventional canonical ensemble sampling.

The results reported in this study provide atomistic level details of conformations and interactions of full-length Aβ40 and Aβ42 inside the catalytic chamber of IDE and will help to elucidate the binding and degradation mechanisms of these critical peptides by this enzyme.

ACKNOWLEDGMENT

Computational resources from the Center for Computational Science (CCS) at the University of Miami are greatly appreciated.

SUPPORTING INFORMATION AVAILABLE

Superposition of the two NMR structures (PDB entries 1IYT and 1Z0Q) of Aβ42 (Figure 1), initial NMR structures of Aβ40 (PDB entry 1AML) and Aβ42 (PDB entry 1IYT) (Figure 2), and most representative structures of Aβ40 (PDB entry 1AML) and Aβ42 (PDB entry 1IYT) derived from a 20 ns simulation in an aqueous medium (Figure 3). This material is available free of charge via the Internet at http://pubs.acs.org.

REFERENCES

1. Mirsky, I. A., and Broth-Kahn, R. H. (1949) The inactivation of insulin by tissue extracts. I. The distribution and properties of insulin inactivating extracts (insulinase). *Arch. Biochem. 20*, 1–9.
2. Duckworth, W. C., Bennett, R. G., and Hamel, F. G. (1998) Insulin degradation: Progress and potential. *Endocr. Rev. 19*, 608–624.
3. Kurochkin, I. (2001) Insulin-degrading enzyme: Embarking on amyloid destruction. *Trends Biochem. Sci. 26*, 421–425.
4. Tseng, B. P., Esler, W. P., Clish, C. B., Stimson, E. R., Ghilardi, J. R., Vinters, H. V., Mantyh, P. W., Lee, J. P., and Maggio, J. E. (1999) Deposition of Monomeric, Not Oligomeric, Aβ Mediates Growth of Alzheimer's Disease Amyloid Plaques in Human Brain Preparations. *Biochemistry 38*, 10424–10431.
5. Neant-Fery, M., Garcia-Ordoñez, R. D., Logan, T. P., Selkoe, D. J., Li, L., Reinstatler, L., and Leissring, M. A. (2008) Molecular basis for the thiol sensitivity of insulin-degrading enzyme. *Proc. Natl. Acad. Sci. U.S.A. 105*, 9582–9587.
6. Kurochkin, I. V. (1998) Amyloidigenic determinant as a substrate recognition motif of insulin-degrading enzyme. *FEBS Lett. 427*, 153–156.
7. Shen, Y., Joachimiak, A., Rosner, M. R., and Tang, W. J. (2006) Structures of human insulin-degrading enzyme reveal a new substrate recognition mechanism. *Nature 443*, 870–874.
8. Kurochkin, I., and Goto, S. (1994) Alzheimer's β-amyloid peptide specifically interacts with and is degraded by insulin degrading enzyme. *FEBS Lett. 345*, 33–37.
9. Hardy, J., and Selkoe, D. J. (2002) They amyloid hypothesis of Alzhemier's disease: Progress and problems on the road to therapeutics. *Science 297*, 353–356.
10. Iversen, L. L., Mortishire-Smith, R. J., Pollack, S. J., and Shearman, M. S. (1995) The toxicity *in vitro* of β-amyloid protein. *Biochem. J. 311*, 1–16.
11. Geula, C., Wu, C. K., Saroff, D., Lorenzo, A., Yuan, M., and Yankner, B. A. (1998) Aging renders the brain vulnerable to amyloid β-protein neurotoxicity. *Nat. Med. 4*, 827–831.
12. Dahlgren, K. N., Manelli, A. M., Stine, W. B., Jr., Baker, L. K., Kraft, G. A., and LaDu, M. J. (2002) Oligomeric and Fibrillar Species of Amyloid-β Peptides Differentially Affect Neuronal Viability. *J. Biol. Chem. 277*, 32046–32053.
13. Pillot, T., Drouet, B., Queille, S., Labeur, C., Vandekerckhove, J., Rosseneu, M., Pincon-Raymond, M., and Chambaz, J. (1999) The Nonfibrillar Amyloid β-Peptide Induces Apoptotic Neuronal Cell Death. Involvement of Its C-Terminal Fusogenic Domain. *J. Neurochem. 73*, 1626–1634.
14. Suo, Z. M., Humphrey, J., Kundtz, A., Sethi, F., Placzek, A., Crawford, F., and Mullan, M. (1998) Soluble Alzheimers β-amyloid constricts the cerebral vasculature in vivo. *Neurosci. Lett. 257*, 77–80.
15. Younkin, S. G. (1995) Eveidence that Aβ42 is the real culprit in Alhzeimer's disease. *Ann. Neurol. 37*, 287–288.
16. Farris, W., Mansourian, S., Chang., Y., Lindsley, L., Eckman., E. A., Frosch, M. P., Eckman, C. B., Tanzi, R. E., Selkoe, D. J., and Guenette, S. (2003) Insulin-degrading enzyme regulates the levels of insulin, amyloid β-protein, and the β-amyloid precursor protein intracellular domain in vivo. *Proc. Natl. Acad. Sci. U.S.A. 100*, 4162–4167.
17. Kim, M., Hersh, L. B., Leissring, M. A., Ingelsson, M., Matsui, T., Farris, W., Lu, A., Hyman, B. T., Selkoe, D. J., Bertram, L., and Tanzi, R. E. (2007) Decreased Catalytic Activity of the Insulin-degrading Enzyme in Chromosome 10-Linked Alzheimer Disease Families. *J. Biol. Chem. 282*, 7825–7832.
18. Leissring, M. A., Farris, W., Chang, A. Y., Walsh, D. M., Wu, X., Sun, X., Frosch, M. P., and Selkoe, D. J. (2003) Enhanced proteolysis of β-amyloid in APP transgenic mice prevents plaque formation, secondary pathology, and premature death. *Neuron 40*, 1087–1093.
19. Miller, B. C., Eckman, E. A., Sambamurti, K., Dobbs, N., Chow, K. M., Eckman, C. B., Hersh, L. B., and Thiele, D. L. (2003) Amyloid-β peptide levels in brain are inversely correlated with insulysin activity levels in vivo. *Proc. Natl. Acad. Sci. U.S.A. 100*, 6221–6226.
20. Cabrol, C., Huzarska, M. A., Dinolfo, D., Rodriguez, M. C., Reinstatler, L., Ni, J., Yeh, L. A., Cuny, G. D., Stein, R. L., Selkoe, D. J., and Leissring, M. A. (2009) Small-Molecule Activators of Insulin-Degrading Enzyme Discovered through High-Throughput Compound Screening. *PLoS One 4*, No. e5274.
21. Turner, A. J., Fisk, L., and Nalivaeva, N. N. (2004) Targeting amyloid-degrading enzymes as therapeutic strategies in neurodegeneration. *Ann. N.Y. Acad. Sci. 1035*, 1–20.
22. Prabhakar, R. (2009) Computational Insights in the Development of Novel Therapeutic Strategies for Alzheimer's Disease (AD). *Future Med. Chem. 1*, 119–135.
23. Im, H., Manolopoulou, M., Malito, E., Shen, Y., Zhao, J., Neant-Fery, M., Sun, C.-Y., Meredith, S. C., Sisodia, S. S., Leissering, M. A., and Tang, W. J. (2007) Structure of substrate-free human insulin-degrading enzyme (IDE) and biophysical analysis of ATP-induced conformational switch of IDE. *J. Biol. Chem. 282*, 25453–25463.
24. Guo, Q., Manolopoulou, M., Bian, Y., Schilling, A. B., and Tang, W. J. (2010) Molecular Basis for the Recognition and Cleavages of IGF-II, TGF-α, and Amylin by Human Insulin-Degrading Enzyme. *J. Mol. Biol. 395*, 430–443.
25. Malito, E., Hulse, R. E., and Tang, W. J. (2008) Amyloid β-degrading cryptidases: Insulin degrading enzyme, presequence peptidase, and neprilysin. *Cell. Mol. Life Sci. 65*, 2574–2585.
26. Malito, E., Ralat, L. A., Manolopoulou, M., Tsay, J. L., Wadlington, N. L., and Tang, W. J. (2008) Molecular Bases for the Recognition of Short Peptide Substrates and Cysteine-Directed Modifications of Human Insulin-Degrading Enzyme. *Biochemistry 47*, 12822–12834.
27. Manolopoulou, M., Guo, Q., Malito, E., Schilling, A. B., and Tang, W. J. (2009) Molecular Basis of Catalytic Chamber-assisted Unfolding and Cleavage of Human Insulin by Human Insulin-degrading Enzyme. *J. Biol. Chem. 284*, 14177–14188.
28. Li, P., Kuo, W. L., Yousef, M., Rosner, M. R., and Tang, W. J. (2006) The C-terminal domain of human insulin degrading enzyme is required for dimerization and substrate recognition. *Biochem. Biophys. Res. Commun. 343*, 1032–1037.
29. Becker, A. B., and Roth, R. A. (1992) An unusual active site identified in a family of zinc metalloendopeptidases. *Proc. Natl. Acad. Sci. U.S.A. 89*, 3835–3839.
30. Perlman, R. K., and Rosner, M. R. (1994) Identification of zinc ligands of the insulin-degrading enzyme. *J. Biol. Chem. 269*, 33140–33145.
31. Matthews, B. W., Jansonius, J. N., Colman, P. M., Schoenborn, B. P., and Dupourque, D. (1972) Three-dimensional structure of thermolysin. *Nature 238*, 37–41.
32. Holland, D. R., Hausrath, A. C., Juers, D., and Matthews, B. W. (1995) Structural analysis of zinc substitutions in the active site of thermolysin. *Protein Sci. 4*, 1955–1965.
33. Pelmenschikov, V., Blomberg, M. R. A., and Siegbahn, P. E. M. (2002) Theoretical study of the mechanism for peptide hydrolysis by thermolysin. *J. Biol. Inorg. Chem. 7*, 284–298.
34. Bora, R. P., Ozbil, M., and Prabhakar, R. (2009) Elucidation of Insulin Degrading Enzyme Catalyzed Site Specific Hydrolytic Cleavage of Amyloid β-Peptide: A Comparative DFT Study. *J. Biol. Inorg. Chem. 15*, 485–495.
35. Amata, O., Marino, T., Russo, N., and Toscano, M. (2009) Human Insulin-Degrading Enzyme Working Mechanism. *J. Am. Chem. Soc. 131*, 14804–14811.
36. Sticht, H., Bayer, P., Willbold, D., Dames, S., Hilbich, C., Beyreuther, K., Frank, R. W., and Rösch, P. (2004) Structure of Amyloid A4-(1−40)-Peptide of Alzheimer's Disease. *Eur. J. Biochem. 233*, 293–298.
37. Crescenzi, O., Tomaselli, S., Guerrini, R., Salvadori, S., D'Ursi, A. M., Temussi, A. P., and Picone, D. (2002) Solution structure of the Alzheimer amyloid β-peptide (1−42) in an apolar microenvironment. Similarity with a virus fusion domain. *Eur. J. Biochem. 269*, 5642–5648.
38. Triguero, L., Singh, R., and Prabhakar, R. (2008) A Molecular Dynamics Study to Investigate the Effect of Chemical Substitutions of Methionine35 on the Secondary Structure of the Amyloid β (Aβ(1−42)) Monomer in Aqueous Solution. *J. Phys. Chem. B 112*, 2159–2167.
39. Shen, L., Ji, H.-F., and Zhang, H.-Y. (2008) Why is the C-terminus of Aβ(1−42) more unfolded than that of Aβ(1−40)? Clues from hydrphobic intercation. *J. Phys. Chem. B 112*, 3164–3167.
40. Nordling, E., Kallberg, Y., Johansson, J., and Persson, B. (2008) Molecular dynamics studies of α-helix stability in fibril-forming peptides. *J. Comput.-Aided Mol. Des. 22*, 53–58.

41. Tomaselli, S., Esposito, V., Vangone, P., van Nuland, N. A. J., Bonvin, A. M. J. J., Guerrini, R., Tancredi, T., Temussi, P. A., and Picone, D. (2006) The α-to-β Conformational Transition of Alzheimer's Aβ-(1−42) Peptide in Aqueous Media is Reversible: A Step by Step Conformational analysis Suggested the Location of β Conformational Seeding. *ChemBioChem 7*, 257–267.
42. Berendsen, H. J. C., van der Spoel, D., and van Drunen, D. (1995) GROMACS: A message-passing parallel molecular dynamics implementation. *Comput. Phys. Commun. 91*, 43–56.
43. Lindahl, E., Hess, B., and van der Spoel, D. (2001) GROMACS 3.0: A package for molecular simulation and trajectory analysis. *J. Mol. Model. 7*, 306–317.
44. Oosteinbrink, C., Villa, A., Mark, A. E., and van Gunsteren, W. F. (2004) A Biomolecular Force Field Based of the Free Entahlpy of Hydration and Solvation: The GROMOCS Force-Field Parameter Sets 53A5 and 53A6. *J. Comput. Chem. 25*, 1656–1676.
45. Berendsen, H. J. C., Postma, J. P. M., van Gunsteren, W. F., and Hermans, J. (1981) Interational Models for Water in Relation to Protein Hydration, D. Reider Publishing Co., Dordrecht, The Netherlands.
46. Miyamoto, S., and Kollman, P. A. (1992) SETTLE: An analytical version of the SHAKE and RATTLE algorithms for rigid water models. *J. Comput. Chem. 13*, 952–962.
47. Hess, B., Bekker, H., Berendsen, H. J. C., and Fraaije, J. G. E. M. (1997) LINCS: A linear constraint solver for molecular simulations. *J. Comput. Chem. 18*, 1463–1472.
48. Darden, T. A., York, D., and Pedersen, L. (1993) Particle mesh Ewald: An N·log(N) method for Ewald sums in large systems. *J. Chem. Phys. 98*, 10089–10092.
49. York, D. M., Wlodawer, A., Pedersen, L. G., and Darden, T. A. (1994) Atomic-Level Accuracy in Simulations of Large Protein Crystals. *Proc. Natl. Acad. Sci. U.S.A. 91*, 8715–8718.
50. Daura, X., van Gunsteren, W. F., and Mark, A. E. (1999) Folding-unfolding thermodynamics of a heptapeptide from equilibrium simulations. *Proteins: Struct., Funct., Genet. 34*, 269–280.
51. Krieger, E., and Vriend, G. (2002) Models@home: Distributed computing in bioinformatics using a screensaver based approach. *Bioinformatics 18*, 315–318.
52. Zheng, L., Chen, M., and Yang, W. (2008) Random walk in orthogonal space to achieve efficient free-energy simulation of complex systems. *Proc. Natl. Acad. Sci. U.S.A. 105*, 20227–20232.